Magnetic field generation in Rayleigh-Taylor unstable inertial confinement fusion plasmas

Bhuvana Srinivasan, Guy Dimonte, and Xian-Zhu Tang

Phys. Rev. Lett. **108**, 165002 — Published 18 April 2012

DOI: 10.1103/PhysRevLett.108.165002

Magnetic Field Generation in Rayleigh-Taylor Unstable ICF Plasmas

Bhuvana Srinivasan, Guy Dimonte, and Xian-Zhu Tang
Los Alamos National Laboratory, P.O. Box 1663, Los Alamos, NM 87545

Rayleigh-Taylor instabilities (RTI) in Inertial Confinement Fusion (ICF) implosions are expected to generate magnetic fields. A Hall-MHD model is used to study the field generation by 2-D single-mode and multimode RTI in a stratified two-fluid plasma. Self-generated magnetic fields are predicted and these fields grow as the RTI progresses via the $\nabla n_e \times \nabla T_e$ term in the generalized Ohm's law. Scaling studies are performed to determine the growth of the self-generated magnetic field as a function of density, acceleration, Atwood number, and perturbation wavelength.

PACS numbers: 52.30.Ex,52.57.Fg, 47.65.Md

Recent experiments using proton radiography[1] observe peak magnetic fields of order 100 T in direct-drive capsule implosions for Inertial Confinement Fusion (ICF)[2, 3]. Such magnetic fields can be generated via the $\nabla n_e \times \nabla T_e$ term in the generalized Ohm's law[4], n_e and T_e being electron number density and temperature. While 100 T magnetic fields are not large enough to affect the implosion hydrodynamics because the plasma thermal energy far exceeds the magnetic energy, they can reduce the electron thermal conduction through the Hall parameter, $\omega_{ce}\tau_e$ when the electron gyro-frequency, ω_{ce}, exceeds the collision frequency, $1/\tau_e$. Electron thermal conduction is predicted to be important[5, 6] in implosions on the National Ignition Facility (NIF) at interfaces between the hot and cold thermonuclear fuel and the plastic ablator. These interfaces are subject to Rayleigh-Taylor instability (RTI) which can generate the misaligned density and temperature gradients necessary for magnetic fields. The magnetic fields in an RTI mixing zone have not been quantified in any systematic manner.

Here, the magnitude and structure of self-generated magnetic fields due to the RTI is studied using Hall-MHD equations[7] in the WARPX (Washington Approximate Riemann Plasma) code[8]. WARPX captures the non-colinearity of the electron density and temperature gradients by explicitly including both ion and electron dynamics as well as self-consistent electric and magnetic fields. A series of RTI simulations is described in which the plasma parameters are varied over the range expected in NIF to estimate a reduced model for the Hall parameter which can then be implemented into a radiation-hydrodynamics code. This is important because ICF design codes do not generally include the plasma effects that best describe the self-consistent electric and magnetic fields. Simulation results presented here suggest that the Hall parameters can exceed unity for NIF conditions and thereby affect electron thermal conduction.

Simulations are performed in a planar 2-D geometry with a stratified RTI plasma using the discontinuous Galerkin method[9]. The Hall-MHD[7] model used is exactly as described in Ref. [10] with a temperature equilibration term[11] to account for some ion-electron collisions, and gravitational terms in the fluid momentum and energy equations. Presently, no viscosity, resistivity, or heat flux is included in the model.

Combining the Ohm's law with Faraday's law,

$$\frac{\partial \mathbf{B}}{\partial t} = \nabla \times \left[\underbrace{\frac{\nabla p_e}{n_e e}}_{\text{I}} - \frac{1}{\mu_0} \underbrace{\left(\frac{\nabla \times \mathbf{B}}{n_e e} \times \mathbf{B} \right)}_{\text{II}} + \underbrace{\mathbf{u}_i \times \mathbf{B}}_{\text{III}} \right] \quad (1)$$

where $\mathbf{u}_i$ is the ion velocity. An ideal gas law is assumed for electrons. Term I is the electron diamagnetic drift term and its curl is responsible for magnetic field generation, $\nabla \times \frac{\nabla p_e}{n_e e} = -\frac{k_B}{e}\frac{\nabla n_e \times \nabla T_e}{n_e}$. Inclusion of electron physics specifically through Term I is essential to generate a magnetic field in the absence of a seed magnetic field. (Single-fluid MHD dynamo can only amplify an existing seed field.) Term II is the Hall term which also brings about two-fluid effects via some cancellation of the magnetic field. Without the Hall term, the magnetic field generated is found to be larger. Term III is the single-fluid MHD dynamo term which becomes significant if there is an in-plane magnetic field. This has implications for 3-D, where the loss of the symmetry in 3D RTI brings a non-vanishing $\mathbf{u}_i \times \mathbf{B}$ (and hence MHD dynamo) which can significantly amplify the magnetic field generated by Term I in late stages of 3D RTI. This letter isolates the effects of the two-fluid terms, I and II, using 2-D simulations. 3-D results will be presented as follow-up work.

RTI simulations are performed here in planar geometry for a range of parameters relevant to ICF ignition[12]. The nominal case is defined such that the 'light' fluid is deuterium fuel near ignition with ion mass m_i, density $n_0 = 10^{31}/\mathrm{m}^3$, and $T_i = T_e = 5$ keV for ions and electrons, respectively. The equilibrium density (n) and pressure (P) profiles for ions and electrons are

$$n = \frac{n_0}{2}\tanh(\frac{\alpha y}{L_y}) + \frac{3}{2}n_0 \quad (2)$$

$$P = -\frac{g m_i}{2}\left[\frac{n_0}{2}\ln\cosh(\frac{\alpha y}{L_y})\frac{L_y}{\alpha} + \frac{3}{2}n_0 y\right] + \frac{3}{2}n_0 k_B T_0 \quad (3)$$

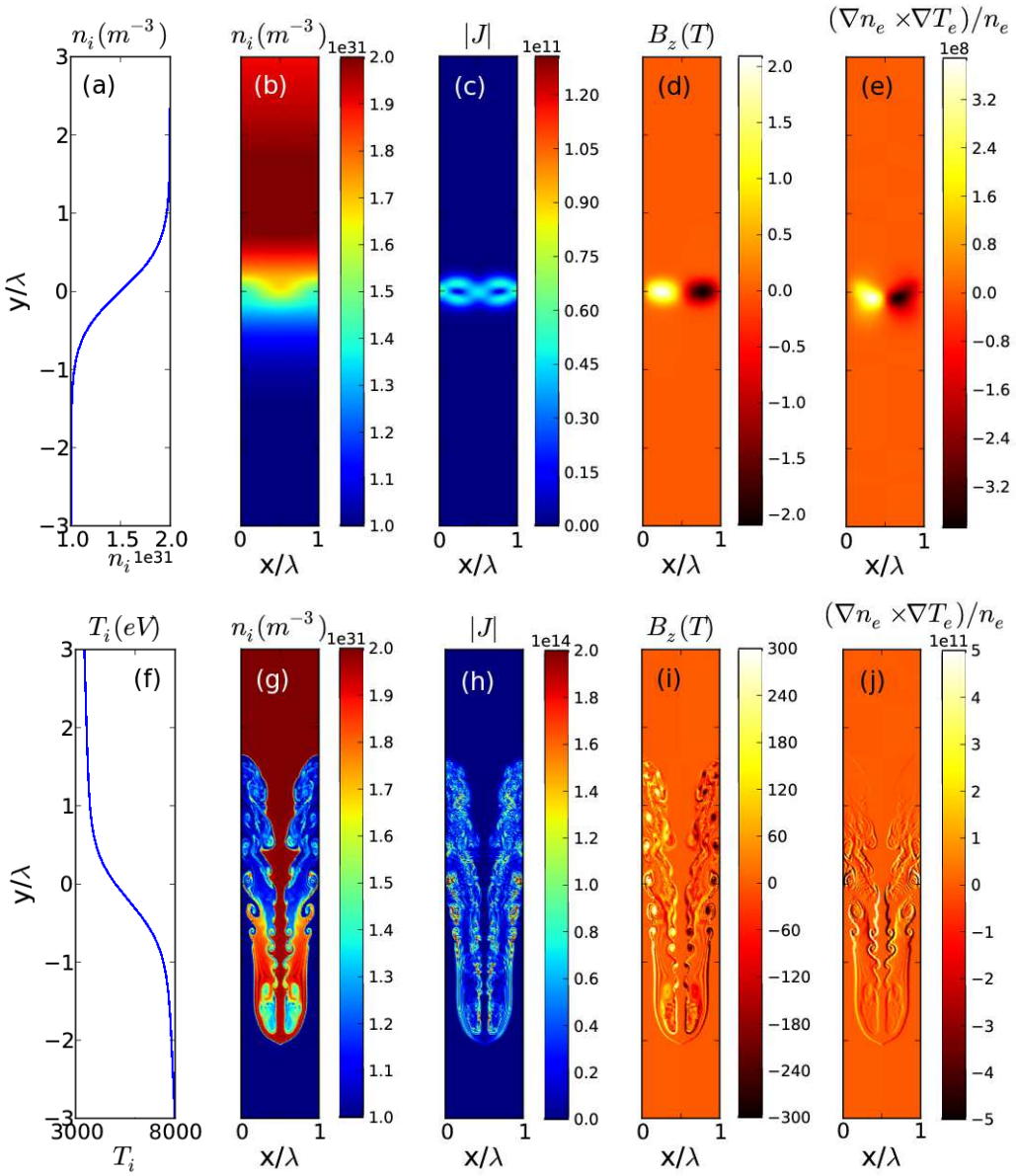

FIG. 1. Initial equilibrium density profile (a) and initial temperature profile (f). Fluid density after $1\tau_{RT}$ (b) and $15\tau_{RT}$ (g). Total in-plane current after $1\tau_{RT}$ (c) and $15\tau_{RT}$ (h). Out-of-plane magnetic field after $1\tau_{RT}$ (d) and $15\tau_{RT}$ (i). $(\nabla n_e \times \nabla T_e)/n_e$ linear approximation after $1\tau_{RT}$ (e) and $15\tau_{RT}$ (j). $1\tau_{RT}$ corresponds to $h/\lambda \approx 0.1$ and $15\tau_{RT}$ corresponds to $h/\lambda \approx 2$. Units for current density in (c) and (h) are A/m^2 and units for (e) and (j) are eV/m^2.

where k_B is the Boltzmann constant, $L_y = 6\lambda$, and $\alpha = 10$ is chosen for a smooth profile with a gradient scale length $\sim \lambda$. Since the RTI in the fuel ice/gas interface occurs in the stagnation phase of an implosion where the fuel radius $\sim 30\mu$m, a wavelength of $\lambda \sim 200\mu$m is used for the nominal case with a representative acceleration $g = 6 \times 10^{13}$m/s^2 and Atwood number $A = 1/3$. The initial vertical y-profiles for n and $T = P/(nk_B)$ are shown in Figs. 1(a) and (f). The horizontal x-profiles are uniform except for a single cosine perturbation at the interface with amplitude in the range of $h_0/\lambda = 0.001 - 0.1$ applied to n. The simulations are performed using $60,000$ cells and a grid convergence study is performed to ensure numerical convergence. Figure 1 shows images of n_i, current density J, out-of-plane magnetic field B_z, and the $\frac{\nabla n_e \times \nabla T_e}{n_e}$ term (using linear approximation) for the nominal case. The time is normalized to the classical RTI growth time, $\tau_{RT} = \sqrt{\frac{1}{Akg}}$. The top row (b)-(e) are at $t = 1\tau_{RT}$ with $h/\lambda \approx 0.1$ and the bottom row (g)-(j) are at $t = 15\tau_{RT}$ with $h/\lambda \approx 2$. In Fig. 1(g), the density exhibits the familiar late-time evolution of the RTI with bubbles, spikes, and Kelvin-Helmholtz (KH) vortices at the edges. Both J and B_z arise in the KH region where the gradients are large and misaligned, as seen in Figs, 1(e) and (j). Horizontal profiles of B_z indicate that the peak magnetic flux bundles that form late in time have a diameter $\delta \sim 0.1\lambda$ for all values of λ that were simulated. The peak field approaches $B_z \sim 10^3$T within these flux bundles, which is not enough to affect the dynamics since the ratio of the thermal to magnetic pressures ($\beta \sim 10^5$) is large. However, such fields can inhibit electron thermal conduction because $\omega_{ce}\tau_e$ can approach unity.

Figure 2 shows the spike and bubble positions (a) and velocities (c) as a function of t/τ_{RT} for the nominal

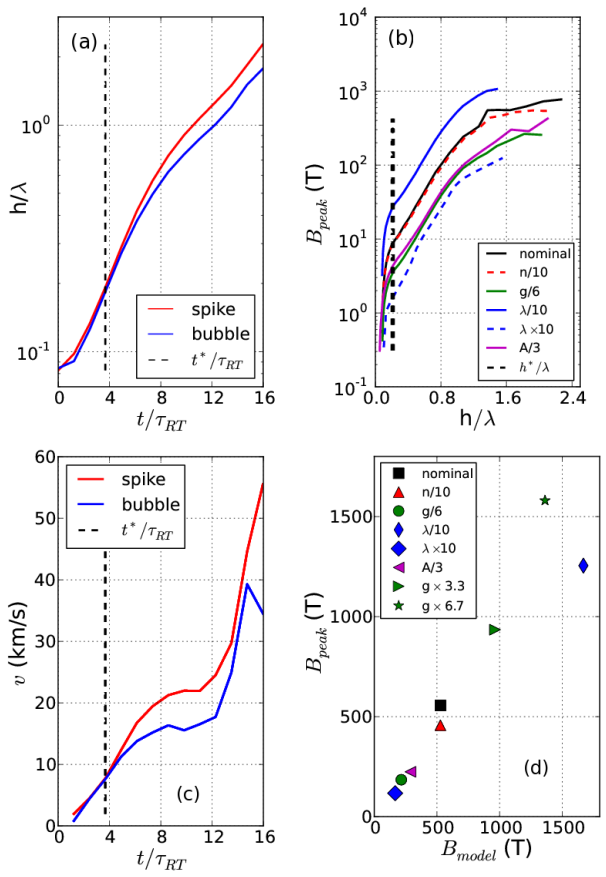

FIG. 2. Spike position as a function of t/τ_{RT} (a), spike velocity as a function of t/τ_{RT} (c), B_{peak} scaling as a function of spike position (h/λ) (b) by varying density, acceleration, wavelength, and Atwood number, and B_{peak} as a function of the model magnetic field (B_{model}) at $h/\lambda \approx 1.5$ (d). t^*/τ_{RT} (with a corresponding h^*/λ and B^*) is when the spike and bubble transition from exponential growth to a terminal velocity stage, which also corresponds to when the dependence of B_{peak} on h/λ goes from linear to exponential.

case. Varying RTI parameters provides similar profiles. At small amplitudes, the spike grows exponentially at $0.64/\tau_{RT}$ where 0.64 is due to the smooth initial profile chosen (described by α in Eq. 2). At the dashed black line marked as t^*/τ_{RT}, the bubble and spike transition from exponential growth to reach terminal velocities of $v_b \approx 17$km/s and $v_s \approx 22$km/s, which are within 12% of those expected[12] in 2-D. Figure 2(c) also shows a re-acceleration of the spike and bubble following the 'terminal' velocity phase due to an increase in vorticity resulting from the Kelvin-Helmholtz instability.

The evolution of B_z is shown in Fig. 2(b) by plotting the peak magnetic field (B_{peak}) vs. the normalized spike amplitude, $\bar{h} \equiv h/\lambda$. For the nominal case (black), B_{peak} grows linearly until about $\bar{h}^* \sim 0.2$ (which implies B_{peak} growing exponentially in time) where $\bar{h}^*$ corresponds to t^*/τ_{RT}. For $\bar{h} > \bar{h}^*$, B_{peak} grows exponentially until $\bar{h} \sim 1$ followed by saturation to a maximum value of ~ 800T at $\bar{h} \sim 1.5$. As the spike and bubble transition to a terminal velocity at $\bar{h}^*$, B_{peak} continues to grow exponentially in time and hence, exponentially in $\bar{h}$.

The other simulations in Fig. 2(b) are performed to understand how B_z varies with RTI parameters. As suggested by term I in Eq. 1, B_{peak} is insensitive to n. The simulations show that B_{peak} can be summarized by

$$B_{model} \sim f(\bar{h}) \frac{m_i}{e} \sqrt{\frac{Ag}{\lambda}} \tag{4}$$

where $f(\bar{h})$ is a universal function for all RTI parameters described in Fig. 4(a). Fig. 2(d) shows the simulation B_{peak} vs B_{model} in Eq. 4 at $\bar{h} = 1.5$.

The results suggest that electron thermal conduction may be inhibited in an RTI mixing region due to self-consistently generated magnetic fields, but in a complex manner. The parameter δ/λ remains constant across different values of λ, δ being the scale-length of B_{peak}. $\delta \sim 10\mu$m, while the electron gyro-radius $\sim 1.6\mu$m which indicates that electrons are magnetized at these scales. This is relevant for the Hall parameter,

$$\omega_{ce}\tau_e = 1.44 \times 10^{16} \frac{T_e^{3/2}}{n} \sqrt{\frac{Ag}{\lambda}} \sim O(0.1 - 1) \tag{5}$$

using B_{model} and the scaling study with λ in m, T_e in eV, g in m/s^2, and n in m^{-3}. $\omega_{ce}\tau_e \sim O(0.1)$ is obtained for the nominal case, and $O(1.0)$ results for $\lambda/10$ and higher g. The Hall parameter indicates that the electron collision time becomes significant for the peak magnetic fields obtained here which can affect electron thermal conduction during NIF ignition. For the regimes explored, the magnetic Reynolds number $Re_m \sim 10^3$ which indicates that magnetic diffusion is negligible with respect to the other time scales in the system.

Simulations are performed to study the magnetic field in the presence of random multiple modes. The initial condition spectrum shown in Fig. 3(c) is of the form $A_M \cos(2\pi(M\frac{x}{L} + \phi_M))$, with mode number $M \in [3, 32]$, amplitude A_M, phase ϕ_M, and domain size L. The multimode solution grows self-similarly[13] and the bubble growth is consistent with previous results[14] $h_b = \alpha_b c_A A g t^2$ where $c_A A \approx 0.64^2 A_{ideal}$ for the smooth gradient, and $\alpha_b \approx 0.06$. c_A accounts for smoothness, and A_{ideal} is the Atwood number for a sharp interface. B_{peak} saturation corresponds with the end of the gt^2 dependence for bubble growth. Figure 3(a) shows early-time evolution and Fig. 3(b) shows late-time evolution of the out-of-plane magnetic field. Varying RTI parameters independently while maintaining the same broadband spectrum, multimode B_{peak} in Fig. 3(d) is summarized by

$$B_{model} \sim f_m(\frac{h}{L}) \frac{m_i}{e} \sqrt{\frac{Ag}{L}} \tag{6}$$

with $f_m(h/L)$ described in Fig.4(b). If run to later in time, a single-mode grows out of the solution as the dominant mode regardless of the initial multimode spectrum.

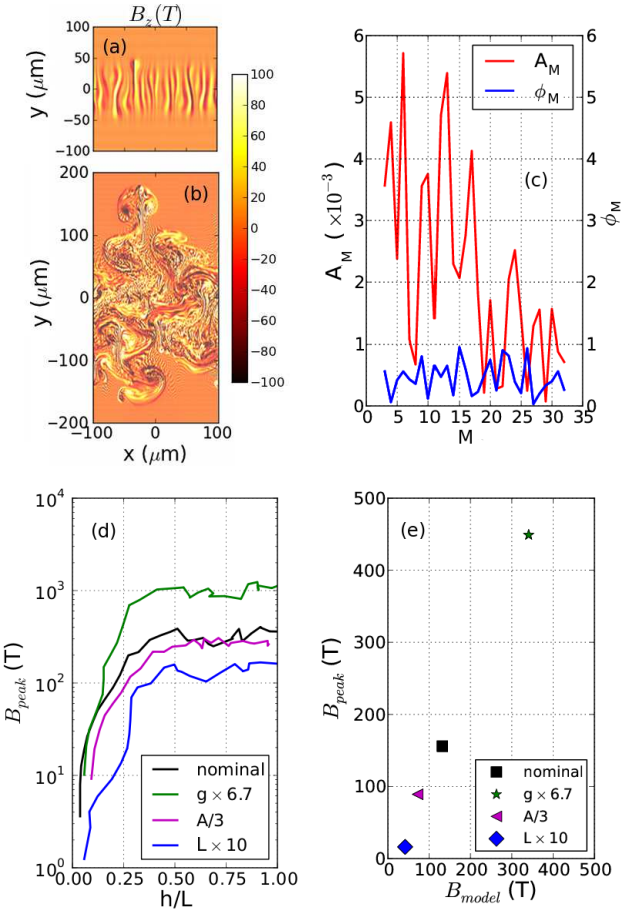

FIG. 3. Early-time evolution (a) and late-time evolution (b) of a random multimode perturbation for out-of-plane magnetic field (B_z), the initial perturbation mode amplitude and phase (c), the peak magnetic field growth as a function of RTI amplitude for several cases (d), and B_{peak} as a function of B_{model} for $h/L \approx 1/5$. The density and temperature profiles have the same morphology as B_z.

The magnetic field appears to follow the fluid interface consistent with observations in the single-mode case. Multimode solutions yield $B_{peak} \sim 300$ T for conditions studied here at $h \sim L$, which is similar to single-mode solutions at $h \sim \lambda$. However, an ICF ignition plasma[15] has a much larger deceleration $g \sim 300-4000$ μm/ns^2, so that $B_{peak} \sim 1.6-6\times10^3$ T from Eq. 6 for $L \sim 100$ μm (hot spot diameter) and $h/L > 1/4$. Then, for a NIF hot-spot, Fig. 4(a) is used in Ref. [16] to estimate $n \sim 10^{24}$ cm^{-3} and $T \sim 3$ keV in the early phase of stagnation ($\rho R \sim 0.01$ g/cm^2), which yields $\omega_{ce}\tau_e \sim 6$. Later at ignition ($\rho R \sim 1$ g/cm^2), $n \sim 10^{26}$ cm^{-3} and $T \sim 20$ keV is estimated so that $\omega_{ce}\tau_e \sim 1$. This suggests that electron heat conduction can be inhibited in NIF by RT generated magnetic fields, but more self-consistent calculations are needed in the future with realistic initial multimode perturbations.

In summary this letter presents two-fluid plasma simulation results that are summarized by Eq. 4 and 5 to estimate the generated magnetic fields and the Hall parameter for ICF Rayleigh-Taylor unstable plasmas. The resulting magnetic fields and scaling studies indicate that the Hall parameter can exceed unity for parameter regimes relevant to NIF. The ICF radiation-hydrodynamic codes that simulate a complete spherical implosion could use the estimate of the Hall parameter provided here to account for more accurate plasma effects specifically, through electron thermal conduction.

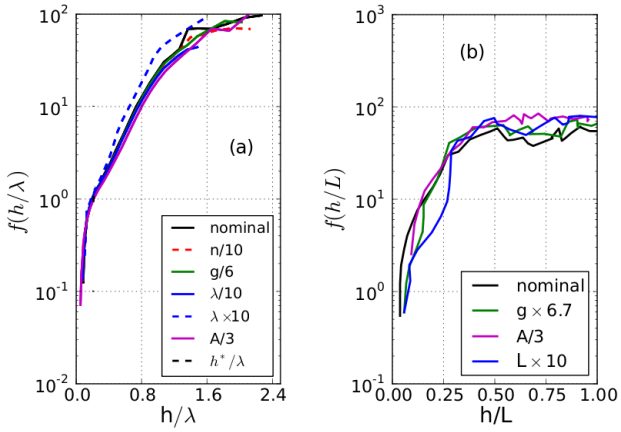

FIG. 4. Single-mode universal $f(h/\lambda)$ (a) and multimode universal $f_m(h/L)$ (b).

The authors wish to acknowledge the code WARPX which was developed at the University of Washington and thank the reviewer for suggesting the sensitivity studies in Ref. [6]. This work was supported by the U.S. Department of Energy at Los Alamos National Laboratory under Contract No. DE-AC52-06NA2-5396.

[1] C. Li *et al.*, Phys. Rev. Lett., **102**, 205001 (2009).
[2] K. Mima *et al.*, Phys. Rev. Lett., **41**, 1715 (1978).
[3] R. Evans, Plasma Phys. Contr. F., **28**, 1021 (1986).
[4] J. Stamper *et al.*, Phys. Rev. Lett., **26**, 1012 (1971).
[5] B. Hammel *et al.*, HEDP, **6**, 171 (2010).
[6] See Supplemental Material at [] for sensitivity studies showing strong dependence of hot-spot temperature on thermal conductivity.
[7] J. Huba, *"Hall-Magnetohydrodynamics - A Tutorial" in Space Plasma Simulations* (Springer, 2003).
[8] U. Shumlak *et al.*, Comp. Phys. Comm., **182**, 1767 (2011).
[9] B. Srinivasan *et al.*, Commun. Comput. Phys., **10**, 183 (2011).
[10] B. Srinivasan and U. Shumlak, Phys. Plasmas, **18**, 092113 (2011).
[11] S. Braginskii, Reviews of Plasma Physics, **1**, 205 (1965).
[12] S. Atzeni and J. Meyer-Ter-Vehn, *The physics of inertial fusion* (Oxford University Press, Inc., 2004).
[13] G. Dimonte and M. Schneider, Phys. Fluids, **12**, 304 (2000).
[14] G. Dimonte *et al.*, Phys. Fluids, **16**, 1667 (2004).
[15] R. Betti *et al.*, Phys. Plasmas, **8**, 5257 (2001).
[16] M. Edwards *et al.*, Phys. Plasmas, **18**, 051003 (2011).